

Spitzer 24 μm Images of Planetary Nebulae

You-Hua Chu¹, Robert A. Gruendl¹, Martin A. Guerrero², Kate Y. L. Su³, Jana Bilikova¹,
Martin Cohen⁴, Quentin A. Parker⁵, Kevin Volk⁶, Adeline Caulet¹, Wen-Ping Chen⁷,
Joseph L. Hora⁸, Thomas Rauch⁹

ABSTRACT

Spitzer MIPS 24 μm images were obtained for 36 Galactic planetary nebulae (PNe) whose central stars are hot white dwarfs (WDs) or pre-WDs with effective temperatures of $\sim 100,000$ K or higher. Diffuse 24 μm emission is detected in 28 of these PNe. The eight non-detections are angularly large PNe with very low $\text{H}\alpha$ surface brightnesses. We find three types of correspondence between the 24 μm emission and $\text{H}\alpha$ line emission of these PNe: six show 24 μm emission more extended than $\text{H}\alpha$ emission, nine have a similar extent at 24 μm and $\text{H}\alpha$, and 13 show diffuse 24 μm emission near the center of the $\text{H}\alpha$ shell. The sizes and surface brightnesses of these three groups of PNe and the non-detections suggest an evolutionary sequence, with the youngest ones being brightest and the most evolved ones undetected. The 24 μm band emission from these PNe is attributed to $[\text{O IV}]$ 25.9 μm and $[\text{Ne V}]$ 24.3 μm line emission and dust continuum emission, but the relative contributions of these three components depend on the temperature of the central star and the distribution of gas and dust in the nebula.

¹*Department of Astronomy, University of Illinois at Urbana-Champaign, 1002 West Green Street, Urbana, IL 61801; chu@astro.uiuc.edu*

²*Instituto de Astrofísica de Andalucía, CSIC. c/ Camino Bajo de Huétor 50, E-18008 Granada, Spain*

³*Stewart Observatory, University of Arizona, Tucson, AZ 85721*

⁴*Radio Astronomy Laboratory, University of California, Berkeley, CA 94720*

⁵*Department of Physics, Macquarie University, Sydney, NSW 2109, Australia*

⁶*Space Telescope Science Institute, 3700 San Martin Drive, Baltimore, MD 21218*

⁷*Institute of Astronomy, National Central University, Chung-Li, Taiwan*

⁸*Center for Astrophysics, 60 Garden St., MS 65, Cambridge, MA 02138*

⁹*Institut für Astronomie und Astrophysik Tübingen (IAAT), Abteilung Astronomie, Sand 1, D-72076 Tübingen, Germany*

Subject headings: circumstellar matter – infrared: stars – planetary nebulae:
general – white dwarfs

1. Introduction

Low- and intermediate-mass stars expel their envelopes to form planetary nebulae (PNe), while their exposed cores evolve into white dwarfs (WDs). The morphology of a PN can be very complex. First of all, a PN may show a multiple-shell morphology due to interactions between fast and slow winds (Kwok 1983) and between the winds and the ambient interstellar medium (Dgani & Soker 1998; Villaver et al. 2003). A bipolar structure may be developed in a PN owing to a fast stellar rotation or close binary interaction (Soker & Livio 1989). Moreover, the effective temperature of the central star of a PN (CSPN) increases as the nebula expands, and the varying stellar UV flux results in varying ionization and excitation structure in the PN (Schönberner 1983). Therefore, images of a PN taken at different wavelengths may exhibit very different morphologies, and comparisons among these images help us understand the PN’s physical conditions and structure.

Infrared (IR) imaging of PNe from the ground is easy at wavelengths $\lesssim 2 \mu\text{m}$, but is hampered by the bright sky background at longer wavelengths. While high-resolution images at wavelengths up to $\sim 20 \mu\text{m}$ can be obtained from the ground for the bright, young, compact PNe (e.g., Volk et al. 2007), it is difficult to observe extended PNe with lower surface brightnesses. The *Spitzer Space Telescope* (Werner et al. 2004) makes it possible for the first time to obtain high-sensitivity images of a large number of older and more extended PNe at near- and mid-IR wavelengths. Its InfraRed Array Camera (IRAC; Fazio et al. 2004) takes images at 3.6, 4.5, 5.8, and $8.0 \mu\text{m}$, while the Multiband Imaging Photometer for *Spitzer* (MIPS; Rieke et al. 2004) takes images at 24, 70, and $160 \mu\text{m}$. IRAC images are available for over 60 PNe and they have detected emission from ionized gas, warm dust, polycyclic aromatic hydrocarbons (PAHs), and H_2 molecular gas (e.g., Hora et al. 2004, 2009; Hora 2009). MIPS images, before our work, were available for only about a dozen mature PNe, excluding proto-PNe that were usually unresolved or saturated in MIPS $24 \mu\text{m}$ images. Analyses of MIPS observations of NGC 650 (Ueta 2006), NGC 2346 (Su et al. 2004), and NGC 7293 (Su et al. 2007) suggest that diffuse emission in the $24 \mu\text{m}$ band is dominated by the [O IV] $25.9 \mu\text{m}$ line, and the 70 and $160 \mu\text{m}$ bands by dust continuum emission.

We have conducted a *Spitzer* MIPS $24 \mu\text{m}$ survey of 72 hot WDs or pre-WDs, selected from McCook & Sion (1999) and Napiwotzki (1999), to search for dust disks at radii of a

few tens of AU (PID 40953). Thirty-six of these hot stars surveyed are still surrounded by visible PNe; therefore, our MIPS survey of hot WDs has provided a three-fold increase of 24 μm images of spatially resolved PNe in the entire *Spitzer* archive. Diffuse emission in the 24 μm band is detected from 28 PNe, among which $\sim 50\%$ show shell morphologies and $\sim 35\%$ show emission only in the central region near the CSPN. In this paper, we describe the observations in Section 2, present the results in Section 3, and discuss the origins of the 24 μm emission in Section 4 and implications of this emission in Section 5.

2. Observations

The MIPS onboard the *Spitzer Space Telescope* was used to image the 36 PNe in the 24 μm band as part of Program 40953. Each object was imaged in the photometry mode using the small offset scale with 10 s exposure time for three cycles. The Basic Calibrated Data processed by the *Spitzer* Science Center’s pipeline software were used to produce mosaics of the PNe. Prior to building each mosaic, bad pixels and latent images of bright point sources in each frame were flagged, and background brightness offsets between individual frames were determined and corrected using the method outlined by Regan & Gruendl (1995). The MOPEX software package was used to combine data and produce the mosaics. The field-of-view of each mosaic covers $\sim 8.0' \times 7.5'$, of which the central $\sim 3.5' \times 3.0'$ portion has a total exposure time of ~ 420 s and the outer regions have exposure times 1/2 or 1/4 that of the center. We note that latent images of the brighter PNe sometimes persist in the outer portions of the final mosaics. The point-spread function of MIPS at 24 μm has a FWHM of $\sim 6''$.

3. Results

Among the 36 PNe that have been imaged in the MIPS 24 μm band, 28 are detected and exhibit a variety of morphologies. To understand the origin of this emission, we compare each PN’s 24 μm morphology to its optical morphology. $\text{H}\alpha$ images, showing all dense ionized gas, are best for such comparison; however, not all PNe have $\text{H}\alpha$ images¹ available, and we

¹ $\text{H}\alpha$ images of MeWe 1-3, HeDr 1, Lo 4, and BLDz 1 are taken from AAO/UKST $\text{H}\alpha$ Survey (Parker et al. 2005); those of MWP 1, NGC 246, and Sh 2-188 were obtained using the Lulin Observatory 1 m telescope; that of NGC 1360 was obtained with the Mt. Laguna 1 m telescope; those of Abell 21, Abell 39, Abell 43, EGB 1, IC 1295, Jn 1, and JnEr 1 are taken from The IAC Catalog of Northern Galactic Planetary Nebulae (Manchado et al. 1996); those of IC 289, NGC 2438, NGC 2610, NGC 3587, and NGC 6852 (published by

have to resort to the Digitized Sky Survey 2 red (DSS2r) images. For PNe with hot CSPNs, the nebular excitation and ionization is high and the strongest emission line in the DSS red passband is the $H\alpha$ line; thus DSS2r images are excellent substitutes for $H\alpha$ images. In one exception, HaTr 7, the DSS 2 blue (DSS2b) image is used because it shows the nebula better than the DSS2r image (Hartl & Tritton 1985). For the rest of the paper, we will loosely use these DSS2r and DSS2b images as “ $H\alpha$ ” images, assuming that they are similar.

Table 1 lists all 36 PNe observed: Column 1, PN name; Column 2, Galactic coordinates; Column 3, CSPN name; Column 4, the stellar effective temperature (T_{eff}); Column 5, the angular size (diameter or major \times minor axes) of the bright main nebula measured from the $H\alpha$ images; Column 6, distance; Column 7, the linear size of the main nebula in $H\alpha$; Column 8, the He II $\lambda 4686/H\beta$ flux ratio; and Column 9, the peak surface brightness at $24\ \mu\text{m}$. The eight PNe that were not detected in the $24\ \mu\text{m}$ images are listed at the end of Table 1.

To visualize the spatial distribution of the $24\ \mu\text{m}$ and $H\alpha$ emission, we have extracted surface brightness profiles along cuts through the nebular center (i.e., the CSPN) at position angles (PAs) selected to avoid contaminating stars and to sample the well-defined shell rims of the main nebula. The width of each cut, typically a few arcsec, has been adjusted to achieve a reasonable signal-to-noise ratio (S/N) in the resulting profile. For each PN, similar widths are used to extract the $24\ \mu\text{m}$ and $H\alpha$ surface brightness profiles, and the profiles are individually zeroed at the background level and normalized to the peak of nebular emission. Note that the $H\alpha$ surface brightness profiles are not normalized in the cases of Abell 61, HaTr 7, and Sh 2-216, because of stellar contamination in the first object and extremely low S/N in the images of the latter two PNe.

Using the images and surface brightness profiles, we find three kinds of correspondence between the $24\ \mu\text{m}$ and $H\alpha$ morphologies of the 28 PNe: (1) the $24\ \mu\text{m}$ emission is more extended than the $H\alpha$ emission, (2) the $24\ \mu\text{m}$ emission has a similar spatial extent as the $H\alpha$ emission, and (3) the $24\ \mu\text{m}$ emission peaks near the CSPN within the $H\alpha$ shell. We have used these different correspondences between $24\ \mu\text{m}$ and $H\alpha$ emission to divide the PNe into three groups accordingly, and arranged them in Table 1 and Figures 1–3 in the order of these groups to facilitate easy comparisons among objects. Some PNe have properties intermediate between Groups 1 and 2, and they are assigned to groups based on larger likelihoods. More detailed descriptions of these groups are given below.

Hajian et al. 1997; Corradi et al. 2000, 2003) have been downloaded from the Image Database of Planetary Nebulae Haloes Web page maintained by Romano L. M. Corradi.

3.1. Group 1

PNe in Group 1 (Figure 1) appear more extended in MIPS 24 μm images than in $\text{H}\alpha$ images. Their images also show sharper outer rims in $\text{H}\alpha$ than at 24 μm , but the differences in sharpness are in part caused by different angular resolutions, $\sim 6''$ for 24 μm and $\leq 2.5''$ for $\text{H}\alpha$. The spatial extent of emission is better illustrated by the surface brightness profiles. Outside the bright shell rim, the 24 μm surface brightness falls off more slowly than the $\text{H}\alpha$ surface brightness, resulting in a vertical offset between the two profiles in Figure 1. The 24 μm emission is also 10–20'' more extended than the $\text{H}\alpha$ emission. These differences cannot be attributed to the poorer instrumental resolution of the 24 μm images. To further illustrate this point, we have convolved the DSS2r image of Abell 15 with a Gaussian of 6'' FWHM, the resolution of the MIPS 24 μm PSF, and plotted the convolved surface brightness profile in a dotted curve in Figure 1. It is clear that the convolved “ $\text{H}\alpha$ ” surface brightness profile is still not as extended as the 24 μm surface brightness profile.

PNe in Group 1 all show similar morphologies at 24 μm : a bright inner shell surrounded by a faint outer envelope; however, the outer envelopes have obvious optical counterparts only in IC 289 and NGC 2610. In the case of NGC 6852, the 24 μm image shows a smooth spherical outer envelope, but its $\text{H}\alpha$ and [O III] images show faint bipolar outer features along PAs of 140° and 320° (Manchado et al. 1996).

3.2. Group 2

PNe in Group 2 (Figure 2) have 24 μm and $\text{H}\alpha$ surface brightness profiles falling off in a similar fashion at the outer rim. Some of these PNe have a well-defined shell morphology, e.g., Abell 39, Abell 43, and NGC 246, but some have irregular shapes or a centrally filled morphology, e.g., HeDr 1 and MWP 1. Overall the morphologies are similar at 24 μm and $\text{H}\alpha$, although the details may differ. For example, Jn 1 shows clear limb-brightening in $\text{H}\alpha$, but appears more filled in at 24 μm . NGC 246 shows enhanced 24 μm emission at $40''$ – $45''$ NW and SE of the CSPN, and its IRAC images also show displaced enhancements along the same PAs (Hora et al. 2004), but no $\text{H}\alpha$ counterparts are seen.

3.3. Group 3

PNe in Group 3 (Figure 3) show diffuse 24 μm nebular emission only in the central region near the CSPN, totally different from the distribution of $\text{H}\alpha$ emission. In the case of NGC 1360, the $\text{H}\alpha$ and 24 μm morphologies are not strikingly different, but the 24 μm

surface brightness profile is much more centrally peaked than the $H\alpha$ profile. A variety of $H\alpha$ morphologies are observed in this group of PNe: thick shells in JnEr 1 and NGC 2438; centrally filled shells in Abell 61, B1Dz 1, HaTr 7, IC 1295, K 1-22, NGC 1360, NGC 3587, and Sh 2-216; semi-circular arcs in Abell 21 and Sh 2-188; and irregular morphology in EGB 1. It is interesting to note that IC 1295, K 1-22, and NGC 3587 show $24\ \mu\text{m}$ emission only near the center of the $H\alpha$ shell, but the $24\ \mu\text{m}$ morphology is strikingly similar to a scaled-down $H\alpha$ morphology. In all three cases, the $24\ \mu\text{m}$ image is bisected by a band of lower surface brightness along the major axis of the $H\alpha$ shell.

3.4. Nondetections

Eight PNe do not show detectable nebular emission in the $24\ \mu\text{m}$ band. Seven of these PNe are angularly larger than the areas that were mapped by the MIPS $24\ \mu\text{m}$ observations (see Column 5 of Table 1), and their surface brightnesses are very low near the CSPNs, where the MIPS observations were centered. There might be some diffuse $24\ \mu\text{m}$ emission in the PN JavdSt 1 (Jacoby & van de Steene 1995), but it is close to the noise level. BE UMa is a cataclysmic variable with a $\sim 3'$ nebular shell (Liebert et al. 1995), which is completely covered by the MIPS $24\ \mu\text{m}$ mosaic, but no diffuse $24\ \mu\text{m}$ emission is detected.

4. Origins of the MIPS $24\ \mu\text{m}$ Emission

What are the origins of the diffuse emission detected in the *Spitzer* MIPS $24\ \mu\text{m}$ band? The $[\text{Ne V}]$ $24.3\ \mu\text{m}$ and $[\text{O IV}]$ $25.9\ \mu\text{m}$ nebular lines and dust continuum are the three main candidates contributing to the MIPS $24\ \mu\text{m}$ fluxes, as indicated by *Infrared Space Observatory* (ISO) SWS spectra of the young PN NGC 7027 and the bipolar PN NGC 2346. In NGC 7027, $[\text{O IV}]$ and $[\text{Ne V}]$ lines and dust continuum are all significant, although the $[\text{Ne V}]$ line is only 1/2 as bright as the $[\text{O IV}]$ line (Bernard Salas et al. 2001). In NGC 2346, the $[\text{O IV}]$ line contributes 27%, and dust continuum contributes the rest of the emission in the MIPS $24\ \mu\text{m}$ band (Su et al. 2004). The excitation potentials of Ne V and O IV are 97.1 and 54.9 eV, respectively. It is not surprising that NGC 7027 and NGC 2346 have such different $[\text{Ne V}]/[\text{O IV}]$ ratios, as the former CSPN has an effective temperature of $\sim 160,000\ \text{K}$ (Beintema et al. 1996) and the latter CSPN has a Zanstra temperature of only $\sim 100,000\ \text{K}$ (Méndez 1978). It is conceivable that the $[\text{Ne V}]/[\text{O IV}]$ ratio increases with stellar temperature, and for CSPNs with effective temperatures $\leq 150,000\ \text{K}$ the $[\text{O IV}]$ $25.9\ \mu\text{m}$ line is by far the strongest emission line in the MIPS $24\ \mu\text{m}$ band.

The ubiquitous presence of [O IV] line emission in our PNe is indicated by the He II $\lambda 4686$ emission that is detected in all available spectroscopic observations of these PNe (see Column 8 of Table 1; compiled by Tylenda et al. 1994). The He II line is emitted through recombinations of He III, of which the excitation potential is 54.4 eV. This excitation potential is close to that of O IV, thus wherever the He II emission is present there ought to be [O IV] emission, as long as the density is not excessively higher than the critical density of [O IV], $\sim 9 \times 10^3 \text{ cm}^{-3}$.

Note that the He II/H β ratios in Column 8 of Table 1 appear to be higher for PNe in Groups 1 and 2 than for those in Group 3, but this is an artificial effect of how the observations were conducted. Optical spectrophotometric observations of PNe are usually made in regions of high surface brightness. For PNe in Groups 1 and 2, the optically bright regions are also bright in the MIPS 24 μm band; however, for PNe in Group 3, the bright 24 μm emission peaks near the center of a nebula, offset from the brightest optical emission in the shell where spectrophotometric observations are made. The He II/H β ratios at the central diffuse 24 μm emission regions should be much higher than those in the nebular shells for Group 3 PNe. The radial variations of the He II/H β ratio, as well as the [Ne V]/[O IV] ratio, reflect the well-known excitation and ionization stratifications in PNe.

The relative importance of nebular line emission and dust continuum in the MIPS 24 μm band depends on the ionization structure and dust content of a PN. It has been illustrated by *Spitzer* IRS observations of PNe in the Large and Small Magellanic Clouds that bipolar PNe are generally dustier than round/elliptical PNe and that the largest PNe exhibit the least dust continuum emission (Stanghellini et al. 2007). Group 1 PNe have 24 μm emission more extended than the H α emission. As [O IV] tracks He II and the He II/H α ratio decreases with radial distance from the CSPN, due to ionization and excitation stratification, the extended emission in the MIPS 24 μm band must be dominated by dust continuum. For the main shells of PNe in Groups 1 and 2, it is likely that both the nebular [O IV] line emission and dust continuum contribute to the MIPS 24 μm flux, but the exact ratios cannot be determined from the current data; spectroscopic observations are needed.

To determine the ratio of line emission to dust continuum for Group 3 PNe, we take a detailed look at *Spitzer* observations of diffuse emission from the Helix Nebula (Su et al. 2007). The IRAC images and MIPS 70 and 160 μm images of the Helix Nebula show the prominent helical ring structure with a hollow center, while the MIPS 24 μm image shows bright diffuse emission in the central region but only faint emission in the helical ring. *Spitzer* IRS observations were made at the central star and its immediate surroundings without additional observations of an external background region. These observations were adequate for deriving a spectrum of the central star but not a spectrum of the nebular

emission because the zodiacal background was bright toward the Helix Nebula. MIPS 24 μm observations indicated that the nebular surface brightness was only about 1/7 that of the zodiacal emission. Indeed, the spectrum of a diffuse emission region near the Helix central star, shown in Figure 4, is dominated by the zodiacal dust continuum emission, and it is not clear whether a small fraction of the dust continuum originates in the Helix Nebula. Nevertheless, the nebular spectrum in Figure 4 shows strong [O IV] 25.9 μm line emission; the [Ne V] 24.3 μm line is much weaker than that of the region encompassing the central star (see Figure 2 of Su et al. 2007).

Recently, we obtained *Spitzer* IRS observations of the CSPN of Sh 2-188 in the mapping mode (PID 50629). While these observations will be presented in another paper, we have used these data to extract a spectrum of the diffuse emission near the central cavity. Figure 5 shows the slit positions marked on a MIPS 24 μm image of Sh 2-188. The spectra extracted from the nebular aperture “Neb” and from the background aperture “Bkg” show significant amounts of dust continuum emission and PAH emission. The origins of this dust continuum and PAH emission are not clear and could be nebular, interstellar, or even zodiacal. The background-subtracted nebular spectrum shows essentially all fine-structure line emission, with the [O IV] line dominating in the MIPS 24 μm band. Therefore, at least in the case of Group 3 PN Sh 2-188 the central diffuse emission in the MIPS 24 μm band is by far dominated by the [O IV] line emission. It is likely that the central diffuse 24 μm emission from all Group 3 PNe is dominated by the [O IV] line. The contribution of [Ne V] line is smaller and depends on the effective temperature of the CSPN and the radial distance to the CSPN.

Finally, we note a complication in NGC 2438. While NGC 2438 is placed in Group 3 with centrally peaked 24 μm emission, diffuse 24 μm emission at lower levels is detected from its nebular shell as well as its halos. As shown in Figure 6, an archival IRAC 8 μm image of NGC 2438 has detected two halos around its main nebular shell, similar to the $\text{H}\alpha$ + [N II] image reported by Corradi et al. (2003); our MIPS 24 μm image of NGC 2438 has detected the main nebular shell and the inner halo clearly, and perhaps some faint emission from the outer halo as well. The IRAC 8 μm band contains strong PAH emission features at 7.7 and 8.6 μm , forbidden lines of [Ar II], [Ar III], [Ar V], and [Ne VI], and weak H I recombination lines, such as $\text{P}\alpha$. Since these halos are detected in all IRAC bands, including the 4.5 μm band that does not include PAH features, it is likely that line emission dominates the near-IR IRAC bands. The 24 μm image of NGC 2438 resembles its [O III] $\lambda 5007$ image (Corradi et al. 2003), suggesting that [O IV] 25.9 μm line emission may make significant contributions to the MIPS 24 μm flux. The relative importance of nebular line and dust continuum emission at 24 μm is unknown. NGC 2438 is projected near the open cluster M46, but their different radial velocities suggest that they are unrelated (Kiss et al. 2008).

5. Implications for PN Evolution

We have defined three groups of PNe according to the spatial extent and surface brightness profile of the $24\ \mu\text{m}$ emission relative to those of the $\text{H}\alpha$ emission. To compare physical properties among these three groups of PNe, we have used the information in Table 1 and plotted the distribution of stellar T_{eff} and nebular sizes in Figure 7. A rough trend of size increase is seen from Group 1 through Groups 2 and 3 to the nondetections, suggesting an evolutionary sequence. The stellar T_{eff} , on the other hand, does not show any obvious trend. This is not surprising because stellar evolutionary tracks bend at the high-temperature extremes and different initial stellar masses lead to different extreme stellar temperatures; thus stellar temperature distributions are not sensitive indicators of evolution.

We have measured the peak $24\ \mu\text{m}$ surface brightness in the shell rim of each PN in Groups 1 and 2 and in the central diffuse-emission region of each PN in Group 3. These surface brightness measurements are listed in Column 9 of Table 1. Two Group 2 PNe, Lo 4 and NGC 246, have peculiar bright spots within their nebular shells; the surface brightnesses of these bright spots are about twice as high as the peak surface brightness in the shell rim. For the PNe that have distances available, we plot their $24\ \mu\text{m}$ surface brightness versus their linear optical sizes in Figure 8. It is evident that the $24\ \mu\text{m}$ surface brightness decreases with nebular size. This correlation is expected from nebular evolution, as nebular expansion leads to lower density and lower surface brightness. Column 9 of Table 1 shows that Group 1 PNe on average have the highest surface brightnesses, and Group 3 PNe have the lowest surface brightnesses. The PNe that do not show detectable diffuse $24\ \mu\text{m}$ emission are still fainter than Group 3 PNe. The trend that the $24\ \mu\text{m}$ surface brightness decreases from Group 1 through Groups 2–3 to the non-detections provides further support of an evolutionary sequence among these PNe.

6. Summary

We have obtained *Spitzer* MIPS $24\ \mu\text{m}$ observations of 36 Galactic PNe, and detected diffuse emission in 28 of them. Comparing the $24\ \mu\text{m}$ surface brightness profiles with those in the $\text{H}\alpha$ line, we find the $24\ \mu\text{m}$ emission can be more extended, similar, or present only in the shell center, and divided these PNe into Groups 1–3, respectively. The optical shell sizes and $24\ \mu\text{m}$ surface brightnesses of the PNe observed suggest that Groups 1–3 and non-detections represent an age or evolutionary sequence, with Group 1 being the youngest.

The diffuse emission in the MIPS $24\ \mu\text{m}$ band is attributed to [O IV] $25.9\ \mu\text{m}$ and [Ne V] $24.3\ \mu\text{m}$ lines and dust continuum emission, but the relative proportions of these

three components depend on the nebular excitation and dust content. The extended 24 μm emission in Group 1 PNe is most likely dominated by dust continuum, as high-ionization fine-structure line emission is expected to decline radially outward. Spectroscopic observations are needed to determine the ratio of nebular line emission to dust continuum for the main bodies of PNe in Groups 1 and 2. Using a *Spitzer* IRS spectrum of the central diffuse emission region of PN Sh 2-188, we illustrate that the [O IV] line is by far the dominant contributor to the MIPS 24 μm emission. It is likely that [O IV] line emission, and some [Ne V] line emission for PNe ionized by the hottest central stars, dominates the central diffuse 24 μm emission among all Group 3 PNe.

This research was supported by NASA grants JPL 1319342 and JPL 1343946. MAG acknowledges support by grants AYA2005-01495 of the Spanish Ministerio de Educación y Ciencia (MEC) and AYA2008-01934 of the Spanish Ministerio de Ciencia e Innovación (MICINN). We thank the anonymous referee for helpful comments.

REFERENCES

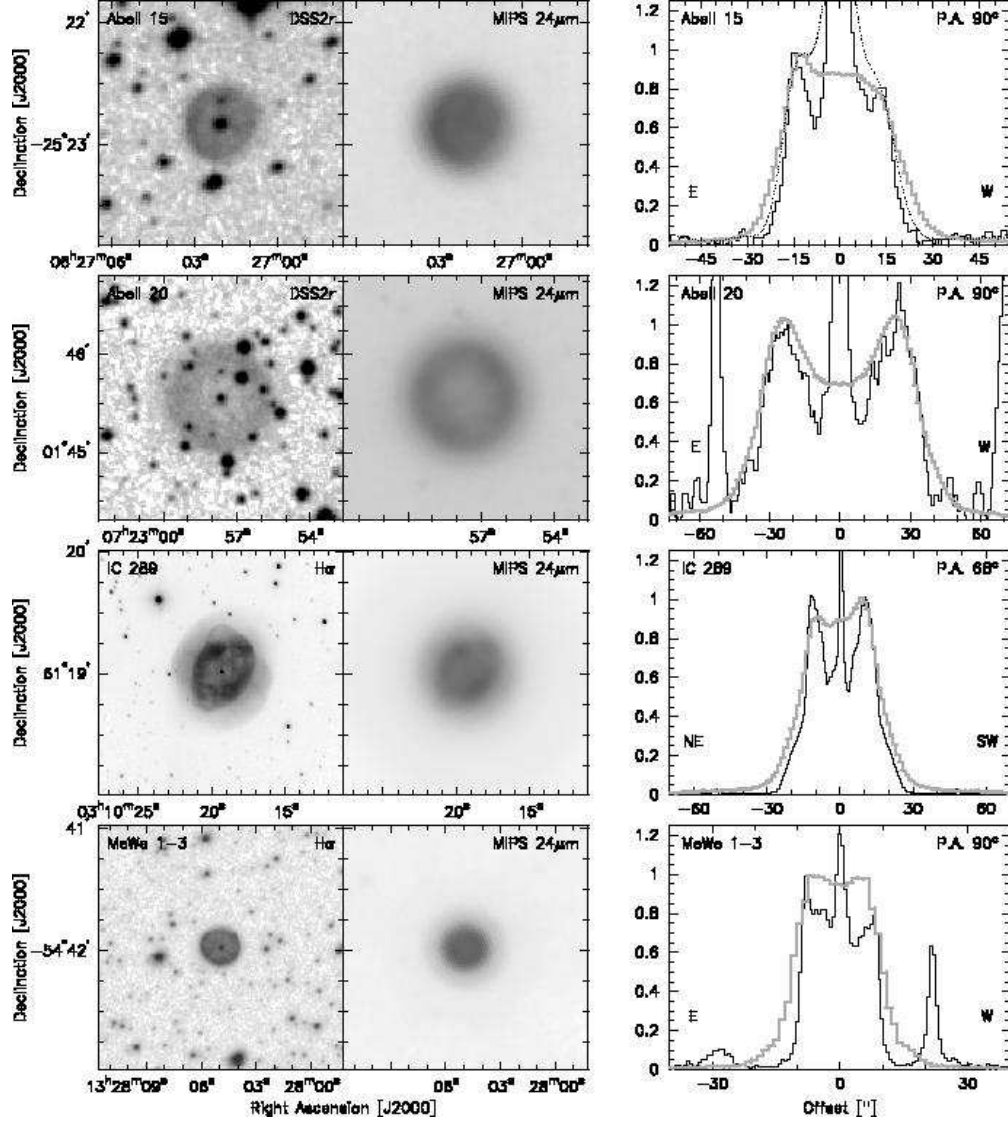
- Beintema, D. A., et al. 1996, *A&A*, 315, L253
- Bernard Salas, J., Pottasch, S. R., Beintema, D. A., & Wesselius, P. R. 2001, *A&A*, 367, 949
- Cahn, J. H., Kaler, J. B., & Stanghellini, L. 1992, *A&AS*, 94, 399
- Corradi, R. L. M., Schönberner, D., Steffen, M., & Perinotto, M. 2000, *A&A*, 354, 1071
- Corradi, R. L. M., Schönberner, D., Steffen, M., & Perinotto, M. 2003, *MNRAS*, 340, 417
- Dgani, R., & Soker, N. 1998, *ApJ*, 495, 337
- Fazio, G. G., et al. 2004, *ApJS*, 154, 10
- Hajian, A. R., Frank, A., Balick, B., Terzian, Y. 1997, *ApJ*, 477, 226
- Harris, H. C., et al. 2007, *AJ*, 133, 631
- Hartl, H., & Tritton, S. B. 1985, *A&A*, 145, 41
- Hora, J. L. 2009, in *Asymmetrical Planetary Nebulae IV*, eds. R. L. M. Corradi, A. Manchado, & N. Soker, Springer-Verlag, 27

- Hora, J. L., Latter, W. B., Allen, L. E., Marengo, M., Deutsch, L. K., & Pipher, J. L. 2004, *ApJS*, 154, 296
- Hora, J. L., Marengo, M., Smith, H. A., Cerrigone, L., & Latter, W. B. 2009, in “The Evolving ISM in the Milky Way and Nearby Galaxies,” *ArXiv e-prints*, 803, arXiv:0803.3937
- Jacoby, G. H., & van de Steene, G. 1995, *AJ*, 110, 1285
- Kiss, L. L., Szabó, G. M., Balog, Z., Parker, Q. A., & Frew, D. J. 2008, *MNRAS*, 391, 399
- Kwok, S. 1983, in *IAU Symp. 103, Planetary Nebulae*, ed. D. R. Flower (Dordrecht: Kluwer), 293
- Liebert, J., Tweedy, R. W., Napiwotzki, R., & Fulbright, M. S. 1995, *ApJ*, 441, 424
- Manchado, A., Guerrero, M. A., Stanghellini, L., & Serra-Ricart, M. 1996, *The IAC Morphological Catalog of Northern Galactic Planetary Nebulae* (La Laguna, Spain: IAC)
- McCook, G. P., & Sion, E. M. 1999, *ApJS*, 121, 1
- Méndez, R. H. 1978, *MNRAS*, 185, 647
- Napiwotzki, R. 1999, *A&A*, 350, 101
- Parker, Q. A., et al. 2005, *MNRAS*, 362, 689
- Regan, M. W. & Gruendl, R. A. 1995, in *ASP Conf. Ser. 77, ADASS IV Proc.*, eds. R. A. Shaw, H. E. Payne, & J. J. E. Hayes (San Francisco, CA: ASP), 335
- Rieke, G. H., et al. 2004, *ApJS*, 154, 25
- Schönberner, D. 1983, *ApJ*, 272, 708
- Soker, N., & Livio, M. 1989, *ApJ*, 339, 268
- Stanghellini, L., et al. 2007, *ApJ*, 671, 1669
- Su, K. Y. L., et al. 2004, *ApJS*, 154, 302
- Su, K. Y. L., et al. 2007, *ApJ*, 657, L41
- Tylenda, R., Stasińska, G., Acker, A., & Stenholm, B. 1994, *A&AS*, 106, 559
- Ueta, T. 2006, *ApJ*, 650, 228
- Villaver, E., García-Segura, G., & Manchado, A. 2003, *ApJ*, 585, L49

Volk, K., Kwok, S., & Hrivnak, B. J. 2007, ApJ, 670, 1137

Werner, K., & Herwig, F. 2006, PASP, 118, 183

Werner, M. W., et al. 2004, ApJS, 154, 1



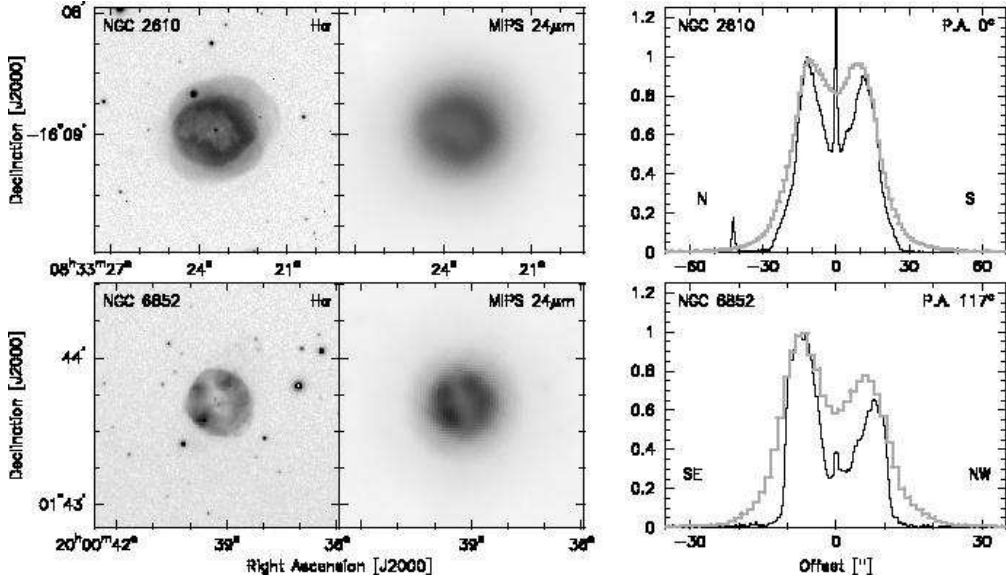
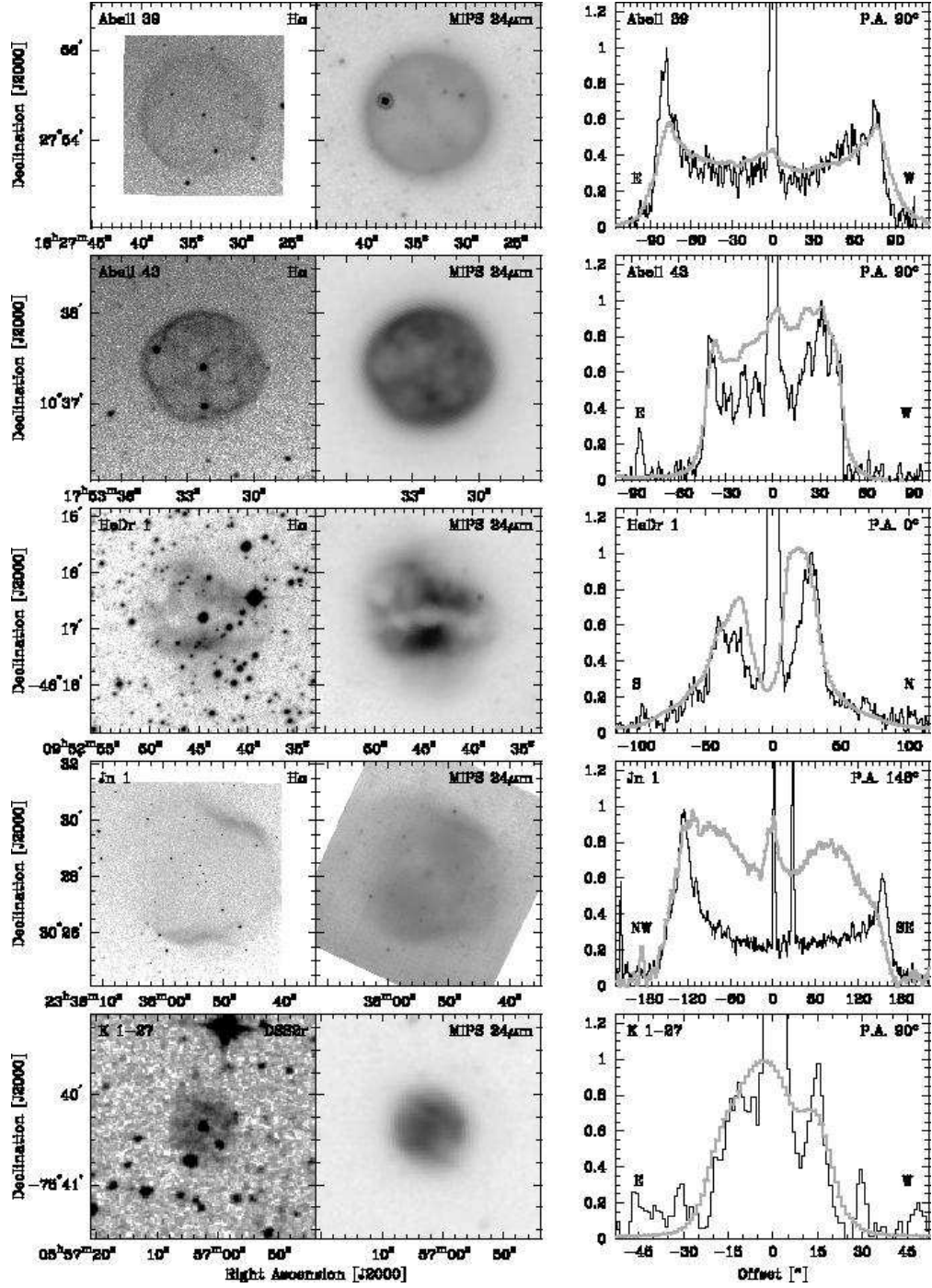


Fig. 1.— Images and surface brightness profiles of Group 1 PNe. The nebula names and passbands are marked on the upper left and right corners, respectively. The surface brightness profiles are extracted through the nebular center along the position angle PA labeled at the upper right corner. The $H\alpha$ surface brightness profile is plotted in black and $24\ \mu\text{m}$ in grey. Note that the “ $H\alpha$ ” surface brightness profiles of Abell 15 and Abell 20 are extracted from DSS2r images. The “ $H\alpha$ ” surface brightness profile of Abell 15 convolved to the $6''$ resolution of the MIPS $24\ \mu\text{m}$ image is plotted in dotted black curve.



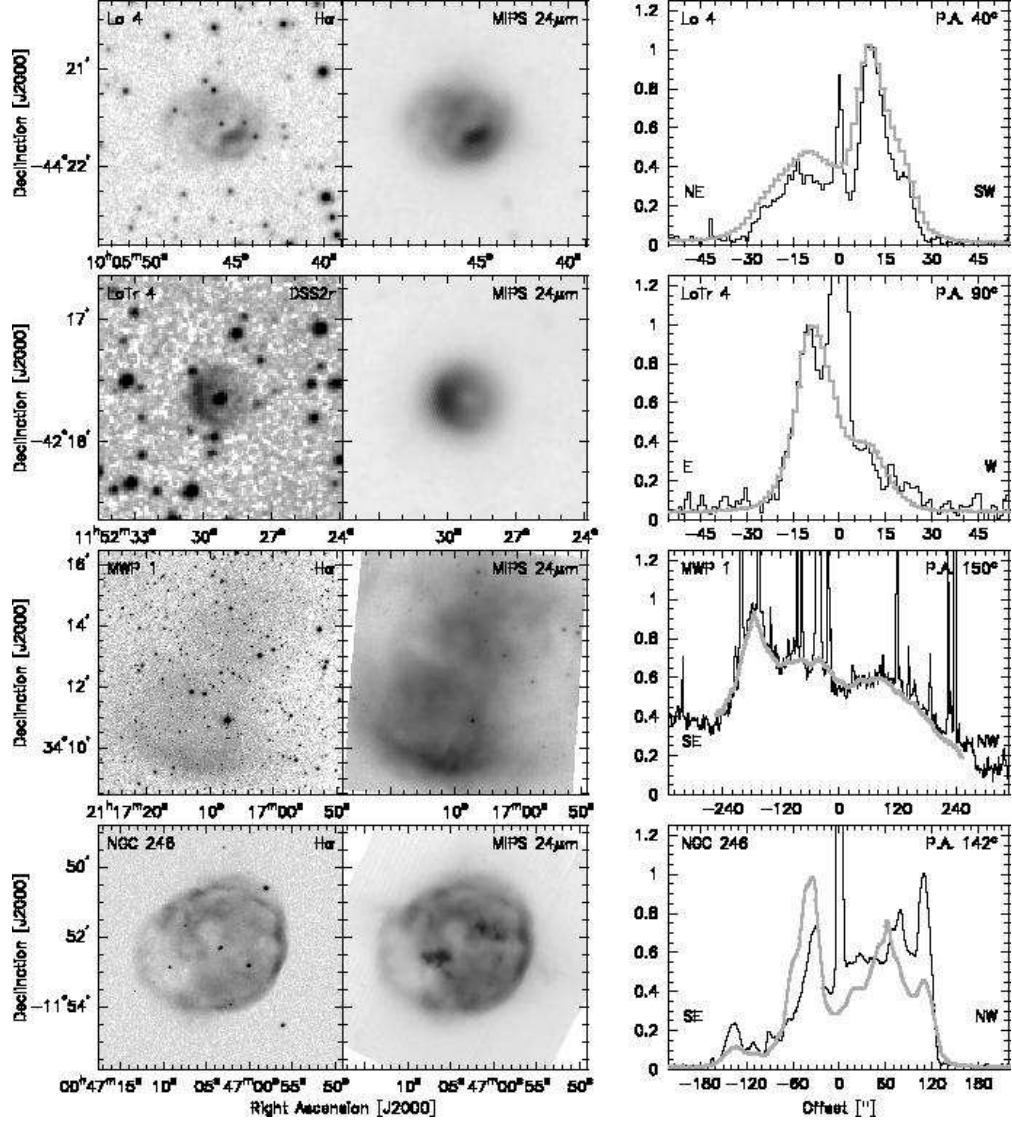
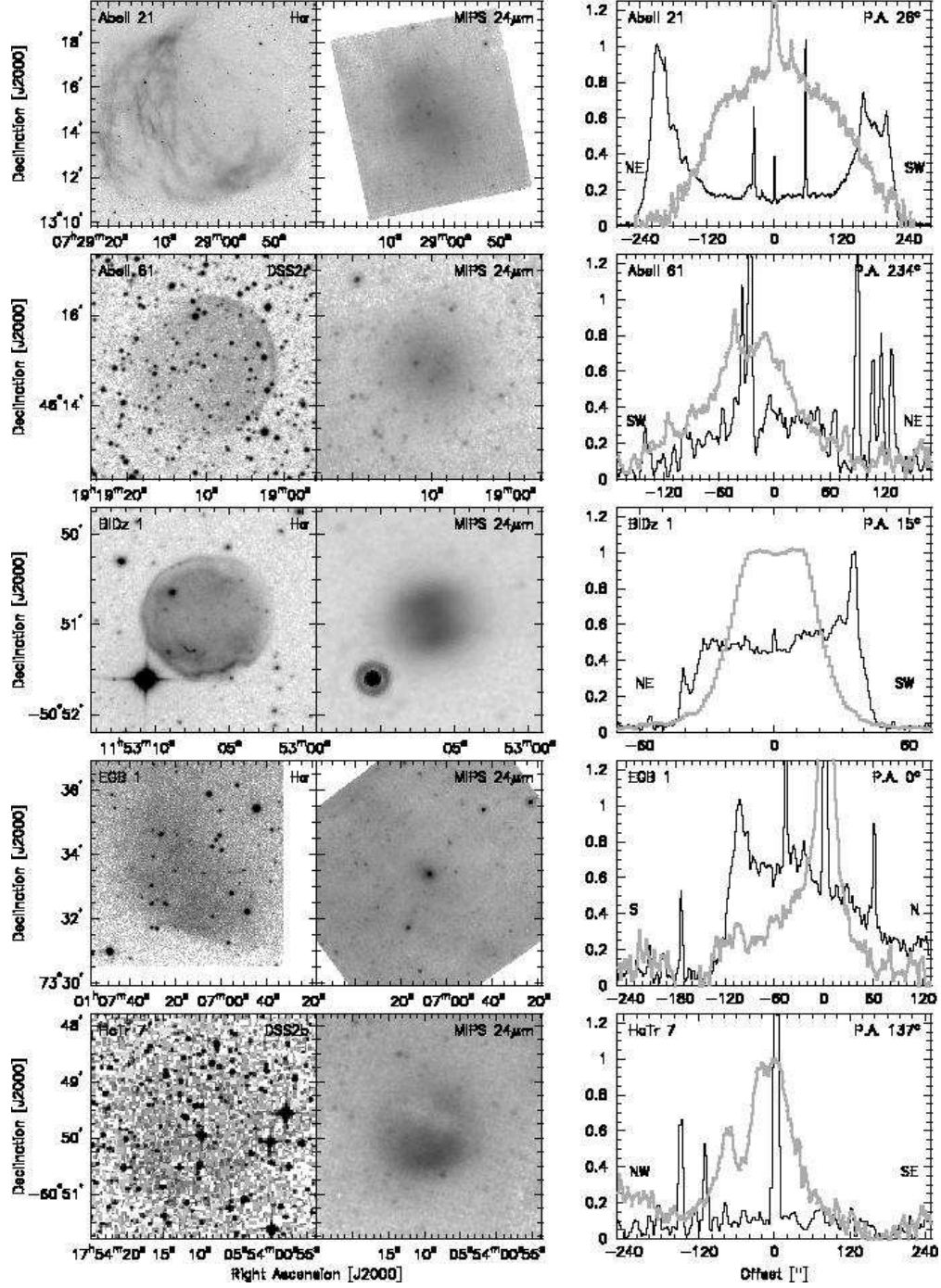
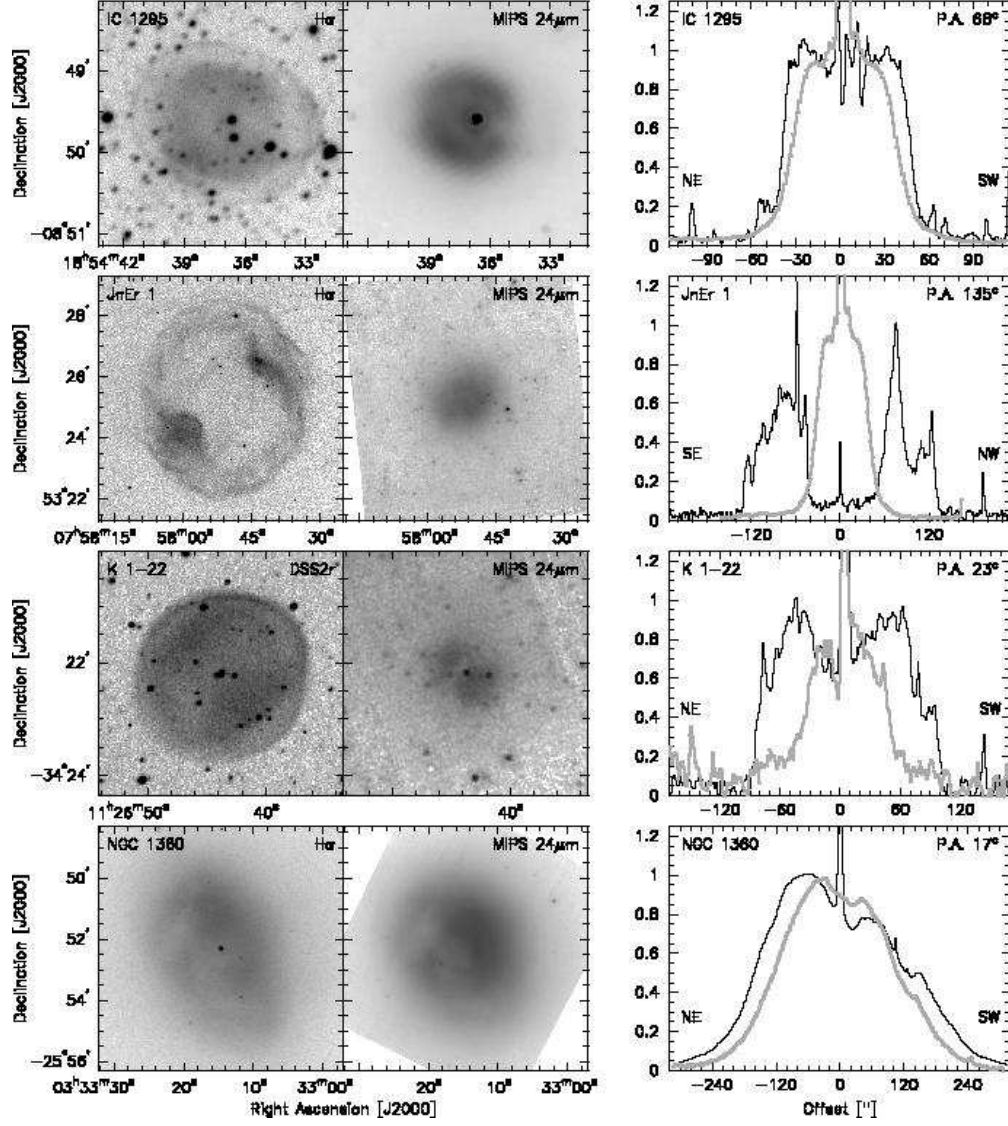


Fig. 2.— Same as Figure 1, but for Group 2 PNe. Note that the “H α ” surface brightness profiles of K 1-27 and LoTr 4 are extracted from DSS2r images.





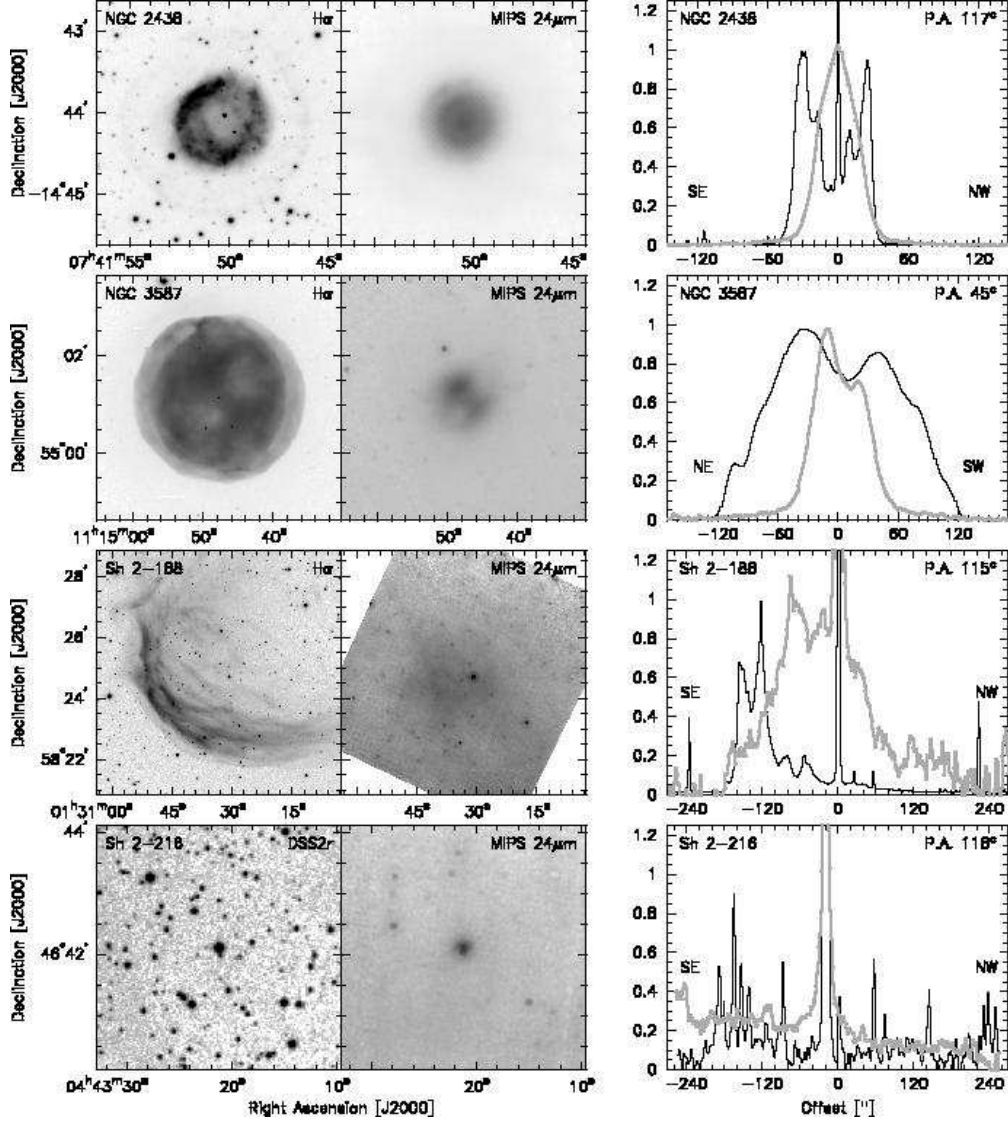


Fig. 3.— Same as Figure 1, but for Group 3 PNe. Note that the “H α ” surface brightness profiles of Abell 61, K 1-22, and Sh 2-216 are extracted from DSS2r images, and HaTr 7 from a DSS2b image.

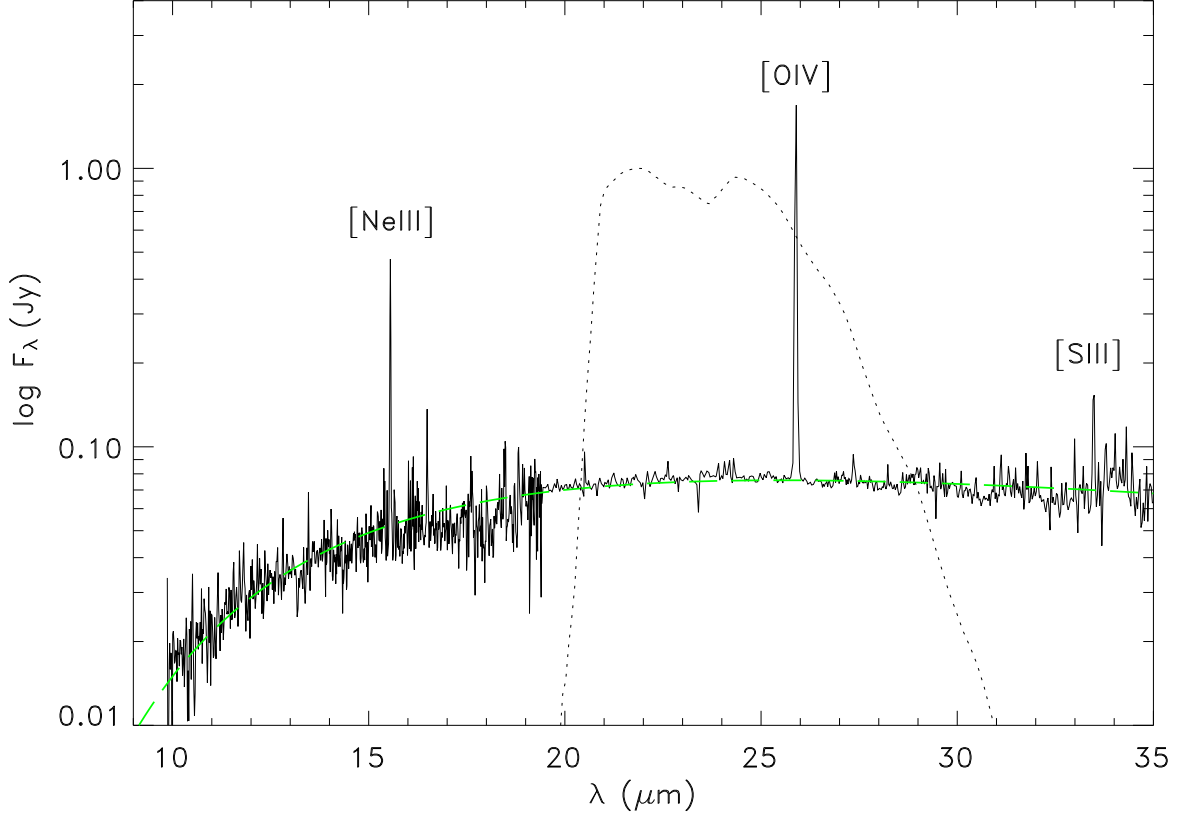


Fig. 4.— *Spitzer* IRS spectrum of the central $24\ \mu\text{m}$ diffuse emission region of the Helix Nebula. No off-source background spectrum was available for zodiacal background subtraction; thus the continuum in the spectrum is dominated by the zodiacal background, which can be approximated by a 200 K blackbody model (dashed curve). The response curve of the MIPS $24\ \mu\text{m}$ band is plotted in a dotted curve.

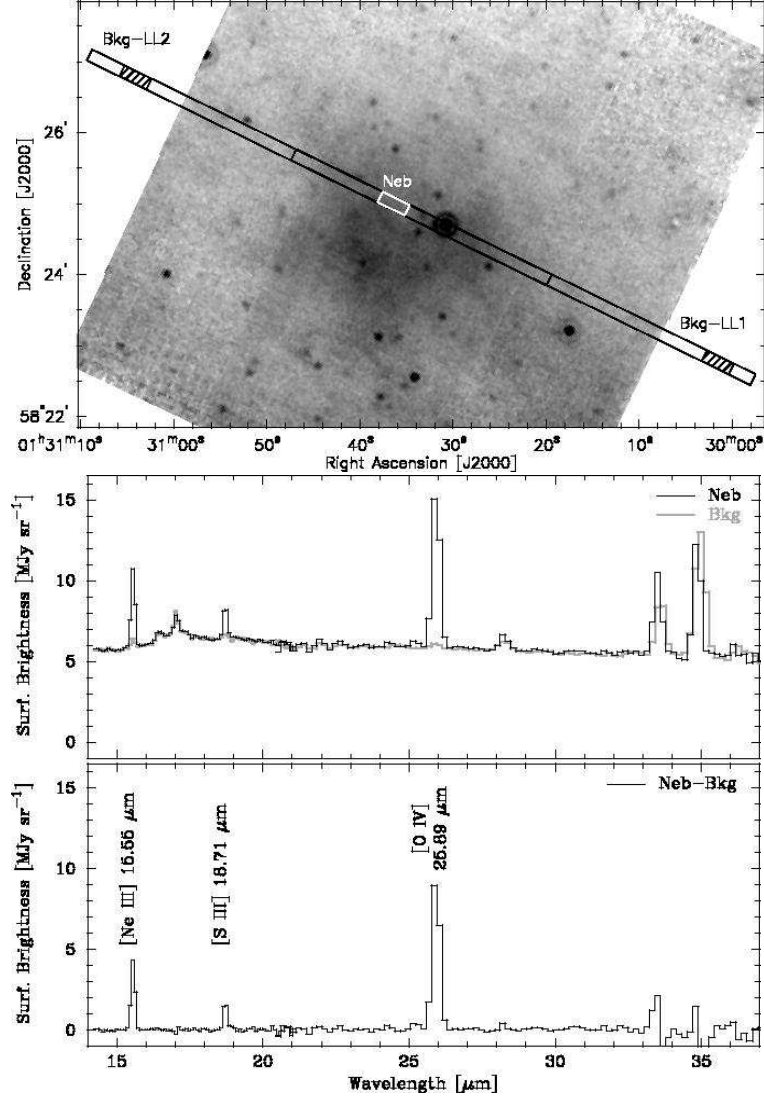


Fig. 5.— *Spitzer* MIPS 24 μm image of Sh 2-188 (top panel) and IRS spectra of the nebula (bottom panels). The nebular and background apertures are marked in the top panel. The LL1 and LL2 spectral modules have different spatial coverages, and thus the background apertures for LL1 and LL2 are different. In the upper spectral panel, the spectrum extracted from the nebular aperture “Neb” is plotted in black, and the background spectrum (LL1 and LL2 combined) is plotted in grey. The background-subtracted nebular spectrum is plotted in the lower spectral panel. The CSPN Sh 2-188 is located near the center of the MIPS 24 μm image, project between a bright foreground star and the nebular aperture.

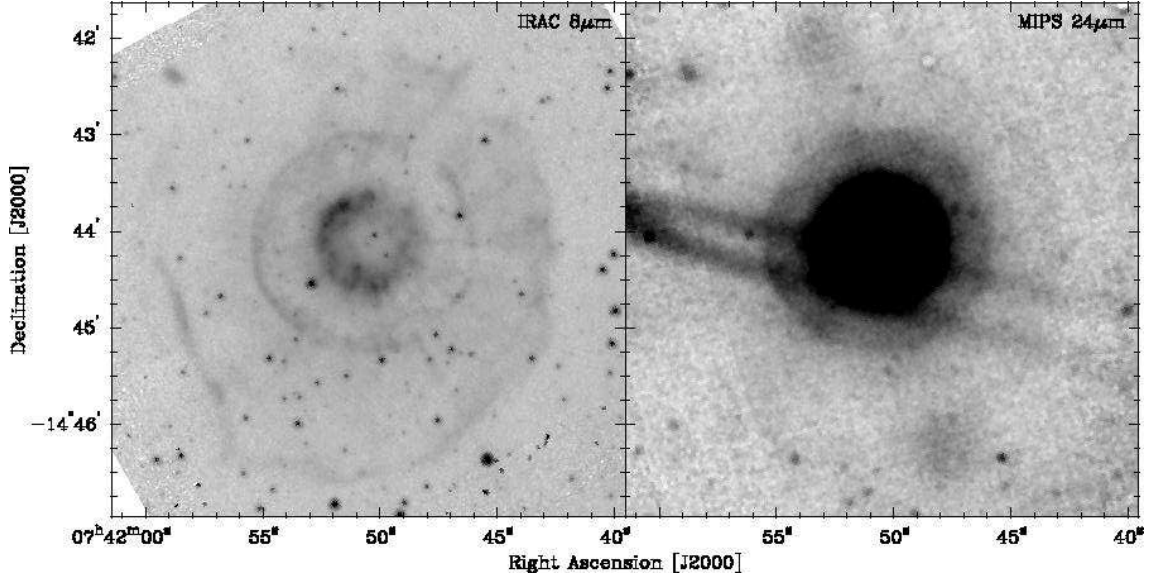


Fig. 6.— *Spitzer* IRAC $8.0\ \mu\text{m}$ and MIPS $24\ \mu\text{m}$ images of NGC 2438. The two stripes of stray light in the $24\ \mu\text{m}$ image is spilled from the Calabash Nebula, a very bright IR source in the post-AGB phase at $\sim 6.5'$ northeast of NGC 2438. The two patches of $24\ \mu\text{m}$ emission at $\text{PAs} = 20^\circ$ and 200° outside the halo are caused by latent images of the bright main nebula.

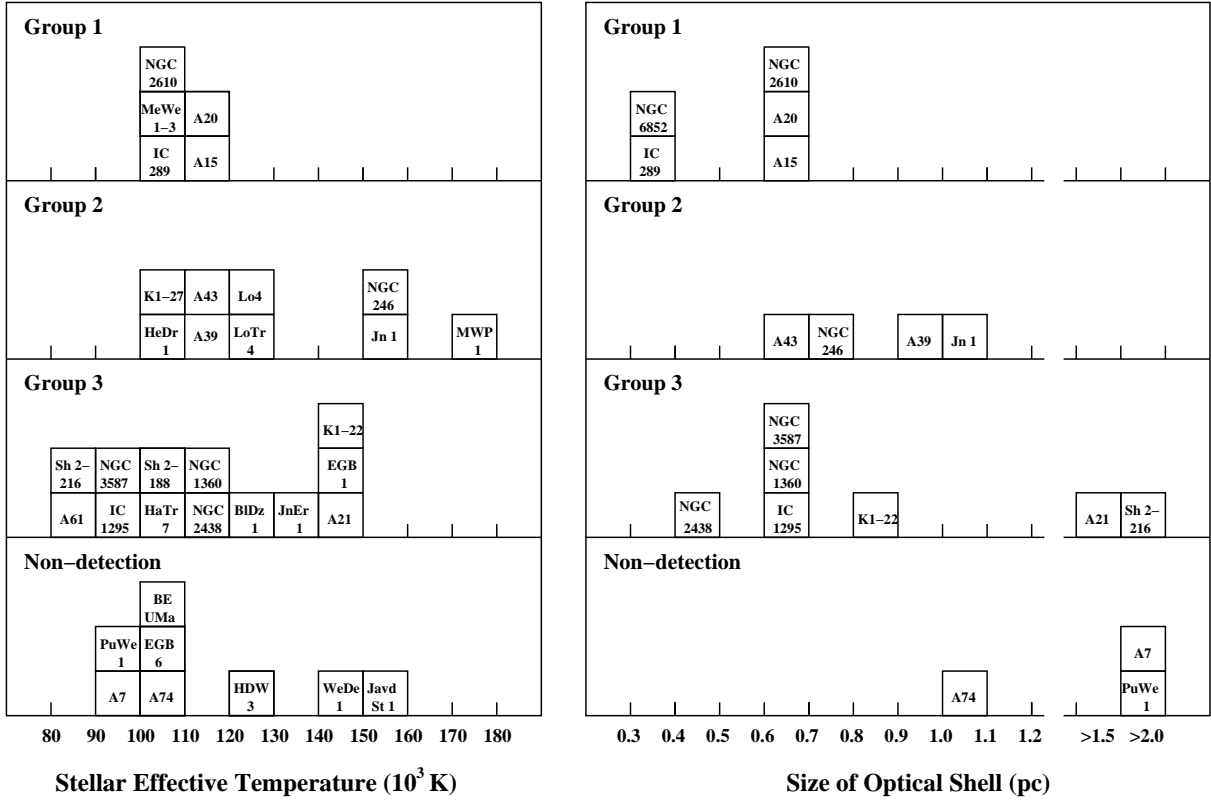


Fig. 7.— Distributions of stellar effective temperatures of the CSPNs and optical ($H\alpha$) shell sizes of the PNe.

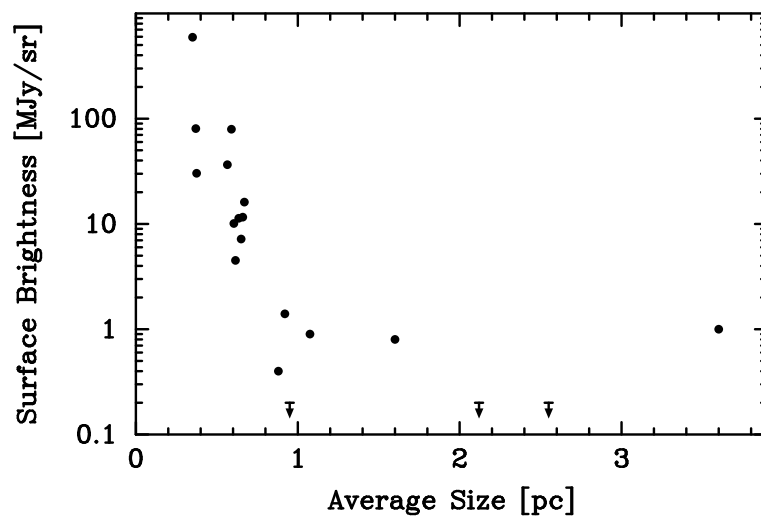


Fig. 8.— Plot of 24 μm surface brightness versus nebular size of PNe that have distances available. The average nebular size is measured from $\text{H}\alpha$ images (Column 7 of Table 1). For non-spherical PNe, the average of the major and minor axes is used.

Table 1. Survey Sample of Hot White Dwarfs and Pre-White Dwarfs

PN Name (1)	PNG Number (2)	CSPN Name (3)	$T_{\text{eff}}^{\text{a}}$ (10^3 K) (4)	Size (arcsec) (5)	Dist. ^b (pc) (6)	Size (pc) (7)	HeII/H β^{c} flux ratio (8)	24 μm SB (MJy/sr) (9)
Group 1								
Abell 15	233.5–16.3	...	110	36×32	3656	0.64×0.57	1.3	10.1
Abell 20	214.9+07.8	...	119	68	1959	0.65	1.5	7.2
IC 289	138.8+02.8	...	100	50	1434	0.35	0.88	593.4
MeWe 1-3	308.2+07.7	...	100	18	27.9
NGC 2610	239.6+13.9	...	100	59×52	2194	0.63×0.55	1.04	79.5
NGC 6852	042.5–14.5	WD 1958+015	...	28	2710	0.37	1.2	80.5
Group 2								
Abell 39	047.0+42.4	WD 1625+280	117	164	1163	0.92	0.69	1.4
Abell 43	036.0+17.6	WD 1751+106	117	85×76	1619	0.67×0.60	0.93	11.3
HeDr 1	273.6+06.1	LS 1362	100	90	13.4
Jn 1	104.2–29.6	WD 2333+301	150	330×295	709	1.13×1.02	0.5	0.9
K 1-27	286.8–29.5	...	105	44	8.7
Lo 4	274.3+09.1	WD 1003–441	120	44	0.9	8.8
LoTr 4	291.4+19.2	...	120	30×26	17.9
MWP 1	080.3–10.4	WD 2115+339	170	300	4.4
NGC 246	118.8–74.7	WD 0044–121	150	273×224	470	0.62×0.51	1.2	36.6
Group 3								
Abell 21	205.1+14.2	WD 0726+133	140	685×530	541	1.8×1.4	0.26	0.8
Abell 61	077.6+14.7	WD 1917+461	88	187	0.6
BlDz 1	293.6+10.9	...	128	88×85	2.6
EGB 1	124.0+10.7	WD 0103+732	147	300×180	0.6:
HaTr 7	332.5–16.9	...	100	198×180	0.9
IC 1295	025.4–04.7	WD 1851–088	90	150×121	1024	0.74×0.60	0.5	16.1
JnEr 1	164.8+31.1	WD 0753+535	130	425×360	0.26	1.1
K 1-22	283.6+25.3	...	141	184	988	0.88	<0.1	0.4
NGC 1360	220.3–53.9	...	110	460×320	348	0.78×0.54	1.0	11.6
NGC 2438	231.8+04.1	...	114	69×60	1203	0.4×0.35	0.4	30.3
NGC 3587	148.4+57.0	WD 1111+552	94	208×198	615	0.63×0.60	0.14	4.5
Sh 2-188	128.0–04.1	WD 0127+581	102	550	0.6
Sh 2-216	158.5+00.7	WD 0439+466	83	5760	129	3.6	...	1.0:
Not Detected								
Abell 7	215.5–30.8	WD 0500–156	99	870×672	676	2.9×2.2	...	<0.2
Abell 74	072.7–17.1	WD 2114+239	108	870×792	752	1.0×0.9	...	<0.2
EGB 6	221.5+46.3	WD 0950+139	100	834	<0.2
BE UMa	144.8+65.8	BE UMa	105	<0.2
HDW 3	149.4–09.2	WD 0322+452	125	540	<0.2
JavdSt 1	085.4+52.3	WD 1520+525	150	660	<0.2
PuWe 1	158.9+17.8	WD 0615+556	94	1200	365	2.12	...	<0.2
WeDe 1	197.4–06.4	WD 0556+106	141	1020×840	<0.2

^aThe stellar effective temperatures are either derived or compiled by Napiwotzki (1999), except those of Abell 21, Jn 1, and JnEr 1, which are from Werner & Herwig (2006).

^bThe distances are from Cahn et al. (1992), except those of Abell 7, Abell 21, Abell 74, PuWe 1, and Sh 2-216 that are from Harris et al. (2007).

^cThe He II $\lambda 4686/\text{H}\beta$ flux ratios are from Tyndea et al. (1994).